Available online at www.sciencedirect.com
ScienceDirect
Journal of Sound and Vibration 303 (2007) 58–77
JOURNAL OF SOUND AND VIBRATION
www.elsevier.com/locate/jsvi

Nonlinear vibration caused by fatigue

Chee-Hoe Foong[a], Marian Wiercigroch[b,*], Ekaterina Pavlovskaia[b], William F. Deans[b]

[a]MCS International Ltd, Exploration House, Aberdeen Science and Energy Park, Bridge of Don, Aberdeen AB23 8GX, UK
[b]Centre for Applied Dynamics Research, Department of Engineering, King's College, University of Aberdeen, Aberdeen AB24 3UE, UK

Received 13 February 2006; received in revised form 7 December 2006; accepted 11 December 2006
Available online 2 March 2007

Abstract

The main aim of this work is to study the interactions between vibration and fatigue crack growth. In this paper, a detailed mathematical modelling of a newly designed fatigue-testing rig, description of the rig, experimental set-up and procedures, and sensor calibrations are presented. The test rig consists of two base-excited oscillators, one positioned above and the other below a single-edge-notched beam sample. The inertial forces of the oscillators act on the sample causing its bending and fatigue. Mathematically the fatigue crack sample is modelled as a discrete spring with piecewise nonlinear stiffness which is assumed to be constant when the crack closes and to decrease with crack length when it opens. The results from the modelling correlate well with the experimental tests.

1. Introduction

In conventional fatigue studies, the stresses used in the life prediction models neglect inertial and damping forces, which implies that the stress is independent of the excitation frequency. In many practical applications, the primary source of dynamic loading does not always act directly on structural components in which a fatigue crack is present. The dynamic loading is transferred by means of inertial forces or oscillations from components of structures to the neighbouring ones. A compelling example is a standard oil-rig, where, fatigue damage often occurs at weld tubular structures of the steel jacket [1,2], process pipe-lines [3] and piles [4]. These structures are continuously subjected to environmental loadings such as waves, wind and current. In reality, vibration and fatigue crack growth are strongly related [5,6], and this relationship is not well understood yet.

The fact that cracks decrease the natural frequency of a structure was reported as early as 1940s by Kirmser [7] and Thomson [8]. This finding implies that, besides the change in structural stiffness, the presence of cracks may also modify structural mass and damping. Consequently, the dynamic characteristics of structures with and without cracks are different. The effects of an opened crack on the changes of natural frequencies have

*Corresponding author. Tel.: +44 1224 272509; fax: +44 1224 272497.
E-mail address: m.wiercigroch@abdn.ac.uk (M. Wiercigroch).
URL: http://wwwcad.eng.abdn.ac.uk/~eng373/.

0022-460X/$ - see front matter © 2007 Elsevier Ltd. All rights reserved.
doi:10.1016/j.jsv.2006.12.008

been studied in [9–15] while other investigations [10,16–27] focused on the effects of a breathing crack. In particular, Papadopoulos and Dimarogonas [12] revealed that the change in natural frequency of a Timoshenko beam of circular cross-section with a transverse surface crack loaded in bending, shear and torsion at its free-end, is small for the first mode of vibration, when the crack location is far away from the clamped-end. Gudmundson [10] derived an opened crack model of a cantilever beam to calculate the eigenfrequencies for different crack lengths and showed that the theoretical and experimental results correlate well. Crack identification including the locality of the crack induced stress field was discussed by Chondros and Dimarogonas in [28,29].

The major critical review in this area [30] was published in 1996, where Dimarogonas has discussed, in detail, various crack modelling methods including the equivalent reduced cross section, local bending moment and the local flexibility methods, crack identifications in beams and rotors, vibration coupling due to the presence of cracks and others. He emphasized the difference between theoretical and experimental studies on real cracks and saw-cuts, and the importance of having a special cracked element in finite elements analysis rather than using a dense mesh.

The main concern of our work is to understand the effects of fatigue crack growth on the dynamic responses of engineering components and structures. Due to the fact that the dynamic responses of a standard cracked specimen are often constrained by the kinematics of the forcing mechanisms in conventional fatigue-testing machines, the natural response of the cracked specimen cannot be easily obtained. Furthermore, a standard single-edge-notched beam (SENB) specimen cannot be tested for zero load crossing in conventional fatigue-testing machines. Therefore, a novel fatigue-testing rig was designed and built; detailed information on the development has been published previously [6,31]. This novel rig consists of two base-excited oscillators, one positioned above and the other below a SENB specimen, and is excited by an electro-dynamic shaker. The main operating principle of the rig is that inertial forces generated by the oscillators act on the specimen. To avoid confusion, it is worth mentioning here that the experimental results obtained in the present work are relevant for a fatigue crack, not a notch.

In this paper, details of comprehensive modelling of the dynamic behaviour of the novel fatigue-testing rig are presented. The description of the rig, operating principle, and experimental set-up are given in Section 2. Three mathematical models describing different loading and contact scenarios are formulated and tested in Section 3, where the SENB specimen is considered crack-free. In Section 4, the SENB specimen is modelled as a spring with piecewise nonlinear stiffness. The stiffness is assumed to be constant when crack closes. When the crack opens the stiffness decreases with crack length and time.

2. Novel fatigue-testing rig and experimental set-up

The fatigue-testing rig, shown in Fig. 1, consists of two base-excited oscillators (masses 1 and 2 of approximately 4 kg each), which are positioned above and below a SENB specimen. Each mass sandwiches a pair of leaf springs, which are also sandwiched and bolted on tower 1. These two pairs of leaf springs prevent the masses from rotating during oscillations, hence, the line of action of the applied force is perpendicular to the neutral axis of the specimen. The stiffness of the leaf springs can be adjusted by sliding tower 1 along the slot on the base, giving a range of stiffness for each pair of 15.65–110.13 kN/m. The test specimen is held by supports at both ends, which are also adjustable to accommodate a range of specimen lengths. The specimen is then in turn held in place on the supports by a means of loading pins.

During testing, both oscillators are kept in contact with the specimen by the aid of the pre-loads from the pneumatic cylinders, having a maximum operating pressure of 10 bar. In addition, the pneumatic cylinders are used to set the prescribed mean load on the specimen by appropriately adjusted pressures at the top and the bottom. With this loading arrangement, fatigue testing with positive (tension), negative (compression) or zero mean stress can be carried out.

During operation, the test rig is mounted on an electro-dynamic shaker. The shaker provides the base excitation in which the inertial forces of both oscillators are generated and act on the specimen. During the downward motion, the inertia of mass 1 exerts a load on the specimen causing the crack to open and the inertia of mass 2 is responsible for closing the crack during the upward motion. The amount of inertial force induced on the specimen is controlled by the adjustment of amplitude and frequency of the base excitation.

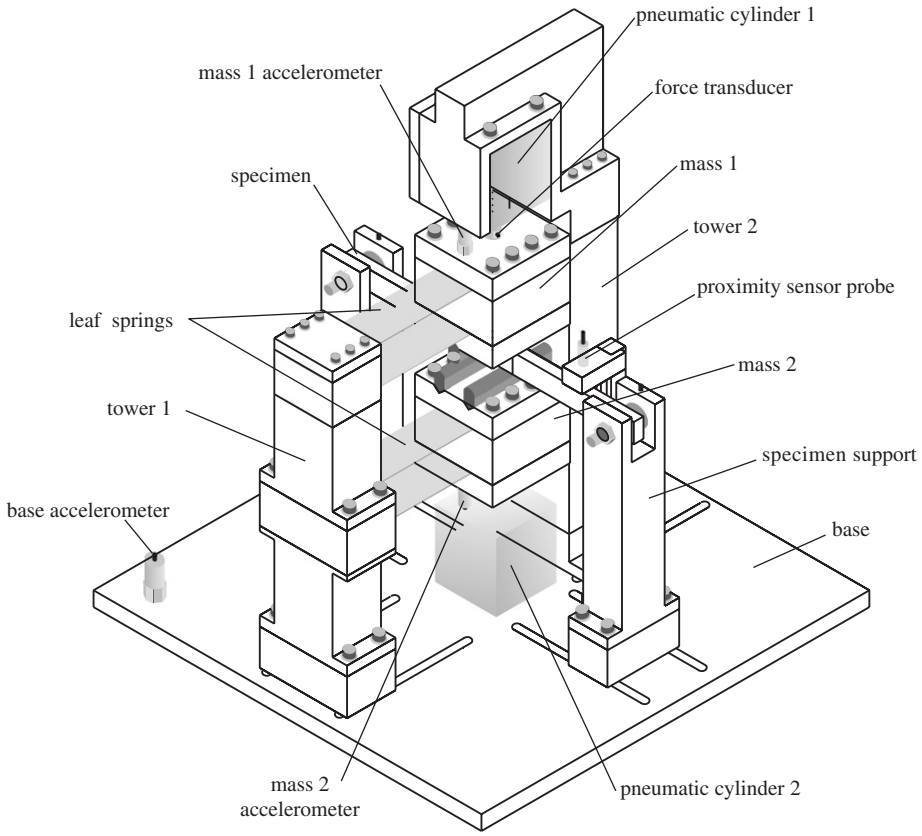

Fig. 1. Novel fatigue-testing rig.

The excitation waveform used to drive the shaker can be periodic or aperiodic (quasi periodic, chaotic or stochastic).

In the present studies, test specimens were manufactured from an aluminium alloy 2024-T351 with the mechanical properties and chemical composition given in Tables 1 and 2, respectively. For all experiments, the same sample type, SENB, was used as shown in Fig. 2 having a width and thickness of 20 and 10 mm, respectively. The depth of the notch was 5 mm long and 1.5 mm wide, and the loading span was 270 mm.

The rig was mounted on the electro-dynamic shaker with the equipment layout as shown in Fig. 3. The base excitation provided by shaker was controlled by the data acquisition unit using *Labview*. The accelerations of the base ($\ddot{x}_b$), mass 1 ($\ddot{x}_{m1}$), and mass 2 ($\ddot{x}_{m2}$), were measured by calibrated accelerometers. A signal from each accelerometer was passed through a charge amplifier and monitored on an oscilloscope before being captured on the data acquisition unit. Similarly, the output of each force transducer (f_{c1} and f_{c2}) was connected to a charge amplifier. Each signal was then passed through an oscilloscope before being captured on the data acquisition unit. The signal of the proximity sensor which represents the relative displacement (z_s) between the specimen and the base was passed through a 1 kHz low-pass filter to remove the high frequency noise. The output of the low-pass filter was then connected to a power supply before being registered on the data acquisition unit. Finally, the signal from the alternating current potential difference (ACPD) crack growth monitor was fed to the data acquisition unit via a power amplifier and an oscilloscope.

In addition to measuring the relative displacement between the test specimen and the base, the proximity sensor was also used to set the dynamic load amplitude of the specimen. For these reasons, the proximity sensor was calibrated to obtain the displacement versus the sensor output voltage and the load versus the sensor output voltage relationships. The displacement calibration procedure was as follow. The central position of the specimen was displaced by a known distance and, at each increment, the output voltage of the proximity sensor was recorded. Since the characteristic of the sensor is entirely linear, the gain factors for the

Table 1
Material properties for aluminium alloy 2024-T351

Property	Value
Tensile strength	454 MPa
Yield strength	317 MPa
Young's modulus	72.4 GPa
Density	2780 kg/m^3

Table 2
Chemical composition for aluminium alloy 2024-T351

AL	Si	Fe	Cu	Mn	Mg	Cr	Zn	Ti
93.63	0.09	0.21	4.06	0.47	1.37	0.01	0.14	0.02

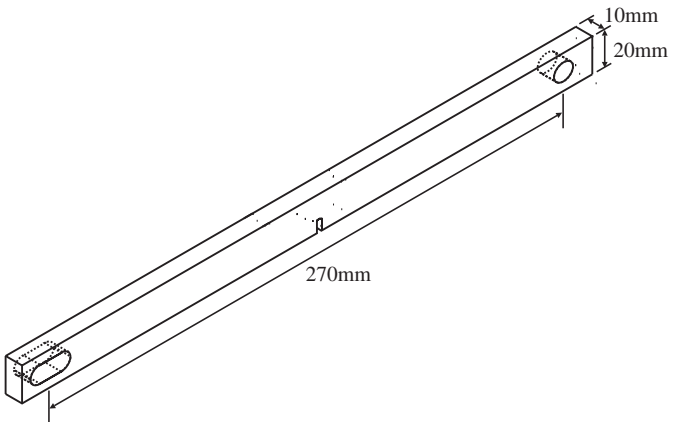

Fig. 2. Geometry of SENB specimen.

aluminium alloys 2024-T351 is 0.171 mm/V. The total compliance, C_{tot}, as a function of crack length of a through-thickness cracked beam can be calculated as [32]

$$C_{\text{tot}} = C_{nc} + C_c, \tag{1}$$

where C_{nc} is the compliance in the absence of a crack and C_c is the additional compliance due to the crack. For the case of a three-point loaded crack-free beam, the compliance, C_{nc}, is given as

$$C_{nc} = \frac{L_{\text{span}}^3}{48EI}, \tag{2}$$

where L_{span} is the loading span, E is Young's modulus, I is the second moment of area ($BW^3/12$), B is the thickness and W is the width of the beam. The compliance, C_c, of the three-point loaded SENB for any value of span-to-width ratio (e.g. $\beta = (L_{\text{span}}/W)$) larger than 2.5 has been developed by Guinea et al. [33] in the following form:

$$C_c = \frac{c_1(\alpha) + \beta c_2(\alpha) + \beta^2 c_3(\alpha)}{EB}, \tag{3}$$

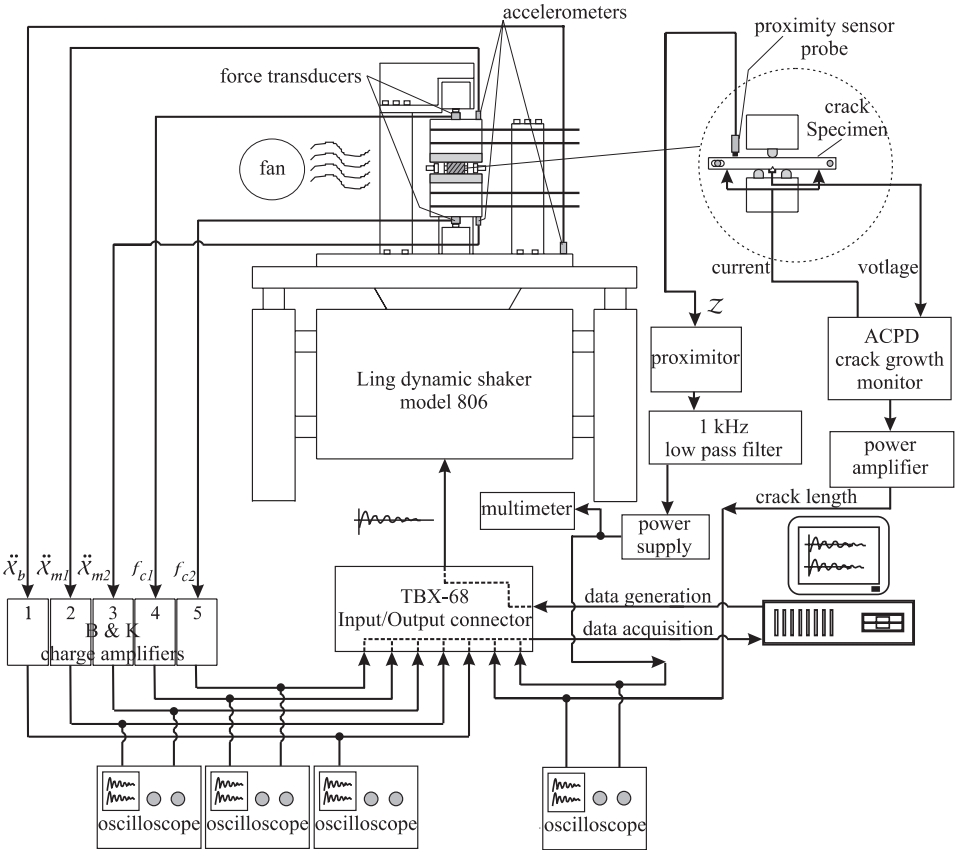

Fig. 3. Experimental layout of the novel fatigue-testing device for inducing dynamic loading.

where

$$c_1(\alpha) = -0.378\alpha^3 \ln(1-\alpha) + \alpha^2 \frac{0.29 + 1.39\alpha - 1.6\alpha^2}{1 + 0.54\alpha - 0.84\alpha^2},$$

$$c_2(\alpha) = 1.1\alpha^3 \ln(1-\alpha) + \alpha^2 \frac{-3.22 - 16.4\alpha + 28.1\alpha^2 - 11.4\alpha^3}{(1-\alpha)(1 + 4.7\alpha - 4\alpha^2)},$$

$$c_3(\alpha) = -0.176\alpha^3 \ln(1-\alpha) + \alpha^2 \frac{8.91 - 4.88\alpha - 0.435\alpha^2 + 0.26\alpha^3}{(1-\alpha)^2(1 + 2.9\alpha)},$$

α is the crack length to specimen width ratio (a/W) where a is the crack length. Substituting Eqs. (2) and (3) into Eq. (1), and rearranging, the load versus sensor output voltage relationship as a function of crack ratio is obtained:

$$P = \frac{(G_f/1000) \times V_{so}}{\dfrac{L_{\text{span}}^3}{48EI} + \dfrac{c_1(\alpha) + \beta c_2(\alpha) + \beta^2 c_3(\alpha)}{EB}}, \tag{4}$$

where G_f is the gain factor (displacement versus sensor output voltage relationship as obtained from above), V_{so} is the sensor output voltage and P is the load. It is worth noting that $(G_f/1000) \times V_{so}$ represents the deflection of the specimen.

A typical test was conducted in the following manner. Before the specimen was pre-loaded, the initial value of the proximity sensor was offset to zero. The amplitude of the proximity sensor output voltage

corresponding to the load amplitudes acting on the specimen was calculated using Eq. (4). The excitation frequency was set to the value of interest and the base amplitude was varied gradually until the amplitude of the output voltage from the proximity sensor coincided with the calculated value.

3. Physical model and equations of motion

In this section, a comprehensive modelling of the dynamic interactions occurring within the novel fatigue testing device for a crack-free specimen is presented. Firstly a single mass model mimicking dynamic bending with pre-load is developed. This is followed by a two mass model which captures the complexity of contact and non-contact regimes. The last part of this section shows how the reduction of the two mass to single mass model can be made.

3.1. Single mass model

When the lower mass is removed, the experimental rig shown in Fig. 1 can be described by the physical model shown in Fig. 4. The mass, m, is attached to two springs and two dashpot dampers, in which k_{Ls} and c_{Ls} represent the stiffness and damping of the leaf spring, respectively, and k_p and c_p are stiffness and damping of the pneumatic cylinder. Both springs are assumed to be linear and the dampers are assumed to be linearly viscous. The masses of the springs and dampers are neglected.

The specimen inertial effects affecting the dynamics of the rig are negligible due to the operating frequency range being much lower than the fundamental frequency of the crack-free specimen. It is assumed that the specimen oscillates in phase with the mass when they are in contact. Therefore, the crack-free specimen is modelled as a discrete linear spring, k_s, with a viscous damping coefficient, c_s. As shown in Fig. 4, the model of the specimen comprises a rigid, massless frame attached to two massless springs of stiffness, $\frac{1}{2}k_s$, and two massless dashpot dampers of viscous damping, $\frac{1}{2}c_s$. It is also assumed that the pre-load induces an elastic deformation at the point of contact between the pneumatic cylinder and the specimen. Physically, the contact stiffness, k_{sc}, as shown in Fig. 4, is many times larger than the stiffness of the specimen, k_s, which means that the displacement of the contact spring is very small.

The static load, P, acting on the mass, m, that is exerted by the pneumatic cylinder and the gravitation force, mg, produces static deflections of the mass, x_m^{st}, and of the specimen, x_s^{st} (see Fig. 4). When mass is in contact with the specimen $x_m^{st} = x_s^{st} = x_s = (P + mg)/(k_{Ls} + k_s)$. The mass is excited harmonically from the base with

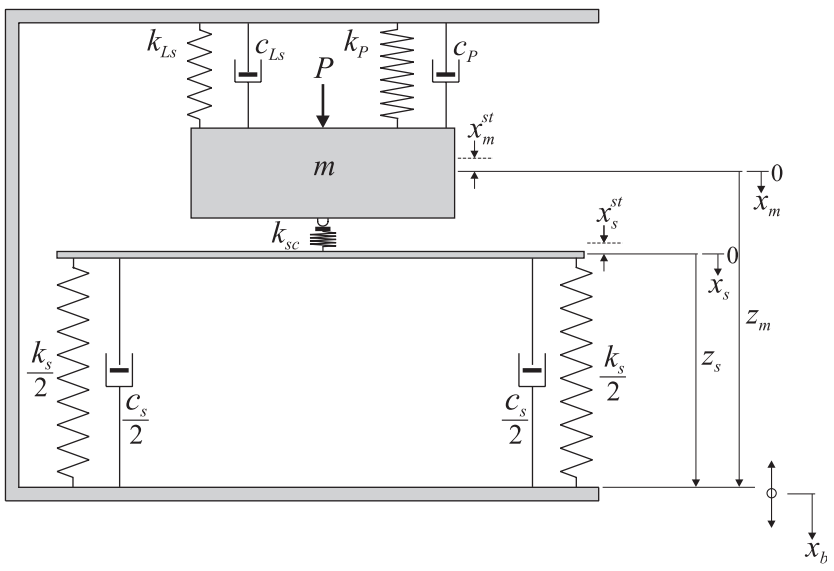

Fig. 4. Model of fatigue-testing rig considering only single mass.

amplitude, A_b, and frequency, Ω. The mathematical model, in the coordinates relative to the base, x_b, when the mass is in contact with the specimen, can be described as

$$m\ddot{z_m} + (c_{Ls} + c_p + c_s)\dot{z_m} + (k_{Ls} + k_p + k_s)z_m = mA_b\Omega^2 \sin(\Omega t), \tag{5}$$

where z_m is the displacement of the mass relative to the base. In Eq. (5), the static load P and the gravitational force mg are compensated by the initial deflections of the springs. When the inertial force of the mass is larger than the static forces, the mass separates from the specimen, which means $z_m < z_s$. The equations of motion are:

$$\begin{aligned} &m\ddot{z}_m + (c_{Ls} + c_p)\dot{z}_m + (k_{Ls} + k_p)z_m + k_{Ls}x^{st} = P + mg + mA_b\Omega^2 \sin(\Omega t), \\ &c_s\dot{z}_s + k_s(z_s + x^{st}) = 0, \end{aligned} \tag{6}$$

where z_s is the displacement of the specimen relative to the base.

Eqs. (5) and (6), are then transformed to sets of first-order differential equations using the following non-dimensional variables and parameters:

$$\tau = \omega_{Ls}t, \quad X_1 = \frac{z_m}{A_b}, \quad X_2 = X_1' = \frac{\dot{z}_m}{A_b\omega_{Ls}}, \quad X_3 = \frac{z_s}{A_b}, \quad X_b = \frac{x_b}{A_b} = \sin(\eta_{Ls}\tau),$$

$$\omega_{Ls} = \sqrt{\frac{k_{Ls}}{m}}, \quad \xi_{Ls} = \frac{c_{Ls}}{2m\omega_{Ls}}, \quad \omega_p = \sqrt{\frac{k_p}{m}}, \quad \xi_p = \frac{c_p}{2m\omega_p},$$

$$\omega_s = \sqrt{\frac{k_s}{m}}, \quad \xi_s = \frac{c_s}{2m\omega_s}, \quad \lambda = \sqrt{\frac{k_p}{k_{Ls}}}, \quad \vartheta = \sqrt{\frac{k_s}{k_{Ls}}},$$

$$\gamma = \frac{x^{st}}{A_b}, \quad f = \frac{P + mg}{mA_b\omega_{Ls}^2}, \quad \eta_{Ls} = \frac{\Omega}{\omega_{Ls}},$$

where $'$ denotes $\mathrm{d}/\mathrm{d}\tau$.

During the *Contact phase*, the displacement of the mass is equal to the displacement of the specimen, $X_1 = X_3$, and the force acting on the mass from the specimen is greater than zero,

$$2\xi_s X_3' + \vartheta X_3 + \vartheta\gamma > 0. \tag{7}$$

The equations of motion in the non-dimensionalised form are:

$$\begin{aligned} &X_1' = X_2, \\ &X_2' = -(1 + \lambda^2 + \vartheta^2)X_1 - (2\xi_{Ls} + 2\xi_p\lambda + 2\xi_s\vartheta)X_2 + \eta_{Ls}^2 \sin(\eta_{Ls}\tau). \end{aligned} \tag{8}$$

For the *No contact phase*, $X_1 < X_3$, the force acting on the mass from the specimen is equal to zero and the following relation holds:

$$2\xi_s X_3' + \vartheta X_3 + \vartheta\gamma = 0. \tag{9}$$

Now the equations of motion are described as

$$\begin{aligned} &X_1' = X_2, \\ &X_2' = -(1 + \lambda^2)X_1 - (2\xi_{Ls} + 2\xi_p\lambda)X_2 - \gamma + f + \eta_{Ls}^2 \sin(\eta_{Ls}\tau), \\ &X_3' = -\frac{\vartheta}{2\xi_s}(X_3 + \gamma). \end{aligned} \tag{10}$$

In Eq. (10), when the mass detaches from the specimen, the velocity of the specimen X_3' decreases to zero.

Next, a set of auxiliary functions, G_1 and G_2 is defined in order to obtain the final form of the equations of motion. The piecewise linear nature of the system can be conveniently described by Heaviside step functions:

$$\begin{aligned} G_1 &= G_1(X_1, X_3) = H(X_1 - X_3), \\ G_2 &= G_2(X_3, X_3') = H(2\xi_s X_3' + \vartheta X_3 + \vartheta\gamma). \end{aligned} \tag{11}$$

Hence, the equations of motion for all possible contact scenarios can be described by the following set of first-order differential equations:

$$\begin{aligned} X_1' &= X_2, \\ X_2' &= -(1+\lambda^2)X_1 - (2\xi_{Ls} + 2\xi_p\lambda)X_2 \\ &\quad - G_1G_2(2\xi_s\vartheta X_2 + \vartheta^2 X_3 + \vartheta^2\gamma) - \gamma + f + \eta_{Ls}^2 \sin(\eta_{Ls}\tau), \\ X_3' &= G_1G_2X_2 + (1-G_1)(1-G_2)\left[-\frac{\vartheta}{2\xi_s}(X_3+\gamma)\right]. \end{aligned} \tag{12}$$

In Eq. (12), the auxiliary functions G_1 and G_2 work as switches; when the mass is in contact with the specimen they are equal to 1 or otherwise 0.

The steady-state time histories computed from Eq. (12) are compared with the experimental results in Fig. 5. The theoretical time histories showing intermittent contacts between the mass and the specimen for accelerations X_b'' and X_1'' are given in Figs. 5a and c, respectively. The displacements of the mass X_1 (dotted line) and of the specimen X_3 (solid line) are plotted on the same graph as shown in Fig. 5e. These time histories were computed for the following values of the system parameters: $\eta_{Ls} = 2.2$, $\xi_{Ls} = 0.00255$, $\xi_s = 0.002$, $\xi_p = 0.4$, $\lambda = 2.53$, $\vartheta = 7.828$ and $f = 3.61$. Extracting the time interval $\tau \in [578.6, 582.5]$ from Fig. 5e, the phases of *Contact* and *No contact* between the mass and the specimen can be clearly distinguished (Fig. 6b), when the mass is in contact with the specimen, both displacements are equal. If the displacement of the mass is larger than the static deflection γ, it separates from the specimen.

The experimental time histories are depicted in Figs. 5b, d and f, where Fig. 5b shows the base acceleration $\ddot{x}_b$, Fig. 5d shows the relative acceleration of the mass $\ddot{z}_m$, and Fig. 5f shows the relative displacements of the mass z_m (dotted line) and of the specimen z_s (solid line). The relative displacement of the mass was obtained by a double numerical integration of the relative acceleration, $\ddot{z}_m$. For this set of tests, the excitation frequency and amplitude were set to 18.31 Hz and 2.48 mm, respectively. The data were acquired at a rate of 5000 samples per second. As the responses of the mass and the specimen were measured by different transducers (accelerometer for the mass and proximity sensor for the specimen) a slight offset of both time histories can be seen, Fig. 5f. Nevertheless, looking at both time histories, it can be deduced that the displacement of the mass is equal to the displacement of the specimen when they are in contact.

It is worth emphasising that the excellent correspondence between experimental and simulated time histories validates the simplifying assumptions made for the constructed model.

3.2. Two mass model

To model the actual fatigue testing rig shown in Fig. 1, a two mass model is needed. The system with two masses allows symmetrical dynamic loading, and it is used for tests that require the specimen to cross zero level loading. Comparing this to the single mass model (Fig. 4), an additional mass m_2 is situated at the bottom of the specimen, as shown in Fig. 7. The mass m_2 is attached to the base in the same way as mass m_1. Here, k_{Ls2} and c_{Ls2} represent the stiffness and damping of the bottom leaf spring, k_{p2} and c_{p2} are the stiffness and damping of the bottom pneumatic cylinder, and k_{sc2} is the contact stiffness between the bottom pneumatic cylinder and the bottom surface of the specimen. To ensure that both masses are kept in contact with the specimen, the pneumatic forces P_1 and P_2 act on masses m_1 and m_2, respectively. As mentioned earlier, the contact stiffnesses (k_{sc1} and k_{sc2}) are many times larger than the stiffness of the specimen k_s, and these springs are needed to determine the *Contact* and *No contact* phases between the masses and the specimen. From the pneumatic forces (P_1 and P_2) and the gravitational forces (m_1g and m_2g), the specimen is loaded from the top and the bottom by $k_{sc1}z_{sc1}^{st}$ and $-k_{sc2}z_{sc2}^{st}$, respectively, where

$$z_{sc1}^{st} = x_{m1}^{st} - x_s^{st}, \quad z_{sc2}^{st} = x_{m2}^{st} - x_s^{st}$$

and, x_{m1}^{st}, x_{m2}^{st} and x_s^{st} are the static displacements of masses m_1, m_2 and the specimen, respectively.

If the pre-loading forces ($P_1 + m_1g$ and $-P_2 + m_2g$) are not large enough to keep both masses in contact with the specimen at all the time, the fatigue rig may operate in one of the following phases: (i) full contact of both masses with the specimen, (ii) partial contact where the mass m_1 loses contact while the mass m_2 is in

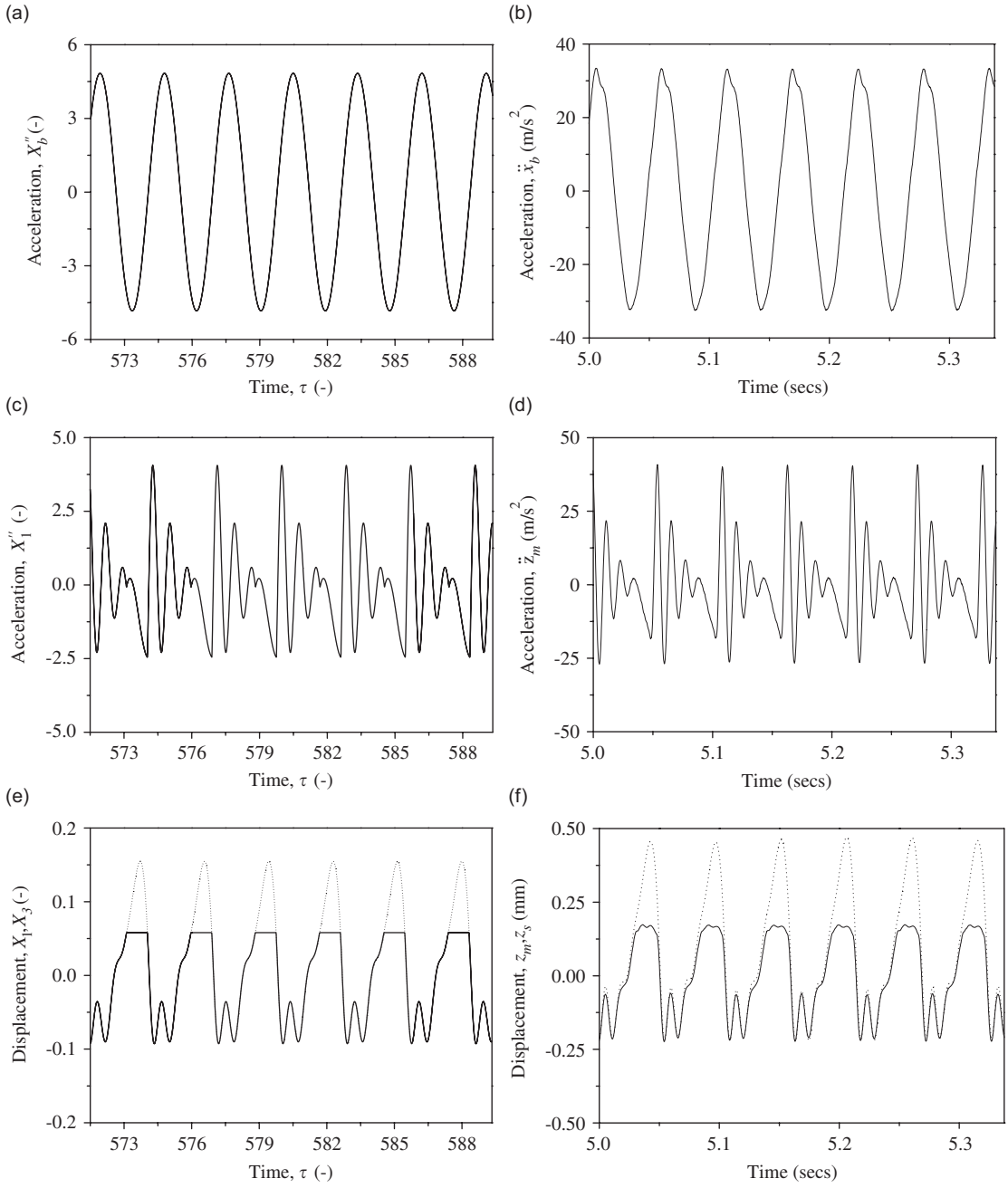

Fig. 5. (a), (c), (e) Theoretical time histories calculated using Eq. (12) for $\eta_{Ls} = 2.2$, $\xi_{Ls} = 0.00255$, $\xi_s = 0.002$, $\xi_p = 0.4$, $\lambda = 2.53$, $\vartheta = 7.828$, $f = 3.61$; (b), (d), (f) Experimental data obtained for excitation frequency of 18.31 Hz and an amplitude of 2.48 mm. Dotted line represents X_1 and z_m, and solid line represents X_3 and z_s in Figs. 5(e) and (f).

contact with the specimen, (iii) partial contact where the mass m_2 loses contact while the mass m_1 is in contact with the specimen, and finally (iv) no contact where both masses lose contact with the specimen. When both masses are in contact with the specimen (phase (i)), the relative displacements of the masses, z_{m1} and z_{m2}, and the specimen, z_s, are oscillating in phase. In addition, if k_{sc1} and k_{sc2} are equal and also if the springs and the dampers that are attached to mass m_1 are identical to those on m_2, then for the considered system the

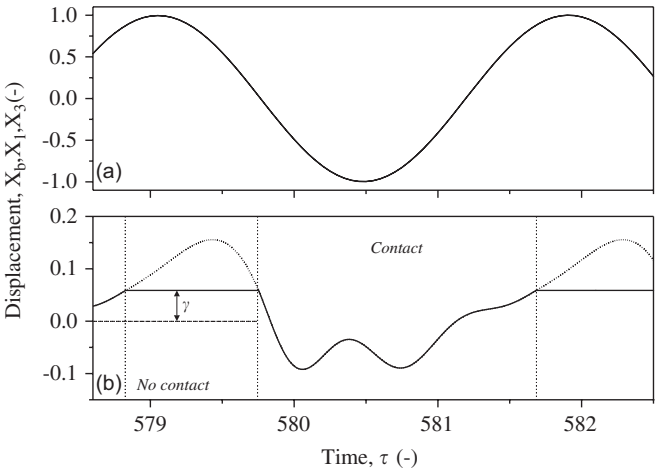

Fig. 6. Time histories for $\tau \in [578.6, 582.5]$: (a) base displacement and (b) from Fig. 5(e) in which dotted line represents X_1 and solid line represents X_3.

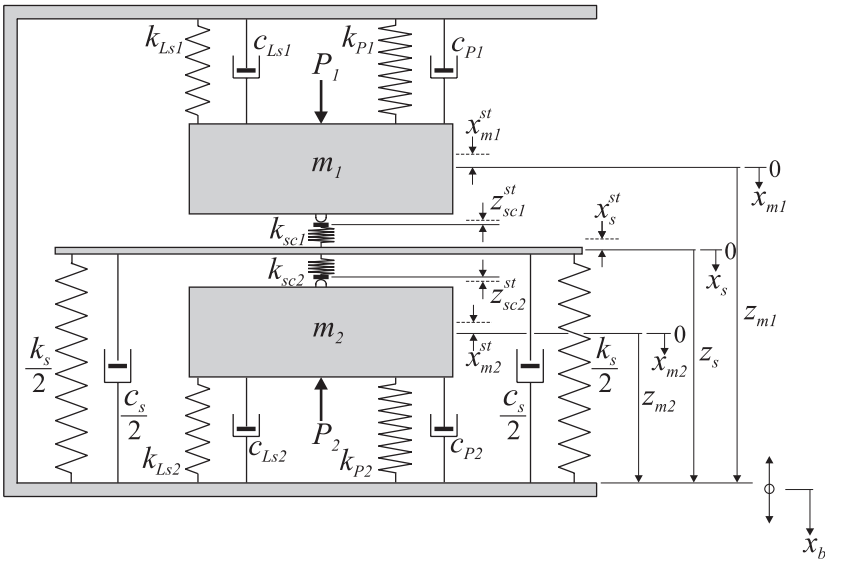

Fig. 7. Symmetric dynamic loading model of the fatigue-testing rig.

displacements of masses m_1 and m_2 are equal, $z_{m1} = z_{m2}$. For phase (i) the equations of motion are:

$$\begin{aligned}
&m_1\ddot{z}_{m1} + (c_{Ls1} + c_{p1})\dot{z}_{m1} + (k_{Ls1} + k_{p1} + k_{sc1})z_{m1} - k_{sc1}z_s = m_1 A_b \Omega^2 \sin(\Omega t),\\
&c_s\dot{z}_s + (k_s + k_{sc1} + k_{sc2})z_s - k_{sc1}z_{m1} - k_{sc2}z_{m2} = 0,\\
&m_2\ddot{z}_{m2} + (c_{Ls2} + c_{p2})\dot{z}_{m2} + (k_{Ls2} + k_{p2} + k_{sc2})z_{m2} - k_{sc2}z_s = m_2 A_b \Omega^2 \sin(\Omega t).
\end{aligned} \tag{13}$$

For phase (ii) to occur, $z_{m1} < (z_s - z_{sc1}^{st})$ has to be satisfied and the force acting between m_1 and the specimen needs to vanish, $k_{sc1}(z_{m1} - z_s + z_{sc1}^{st}) = 0$. Hence the equations of motion are:

$$\begin{aligned}
&m_1\ddot{z}_{m1} + (c_{Ls1} + c_{p1})\dot{z}_{m1} + (k_{Ls1} + k_{p1})z_{m1} + k_{Ls1}x_{m1}^{st} = P_1 + m_1 g + m_1 A_b \Omega^2 \sin(\Omega t),\\
&c_s\dot{z}_s + (k_s + k_{sc2})z_s - k_{sc2}z_{m2} + k_s x_s^{st} - k_{sc2}z_{sc2}^{st} = 0,\\
&m_2\ddot{z}_{m2} + (c_{Ls2} + c_{p2})\dot{z}_{m2} + (k_{Ls2} + k_{p2} + k_{sc2})z_{m2} - k_{sc2}z_s = m_2 A_b \Omega^2 \sin(\Omega t).
\end{aligned} \tag{14}$$

For phase (iii) to occur, $z_{m2} > (z_s - z_{sc2}^{st})$ has to be satisfied and the forces acting between m_2 and the specimen need to vanish; $k_{sc2}(z_{m2} - z_s + z_{sc2}^{st}) = 0$. The equations of motion are then expressed as

$$m_1\ddot{z}_{m1} + (c_{Ls1} + c_{p1})\dot{z}_{m1} + (k_{Ls1} + k_{p1} + k_{sc1})z_{m1} - k_{sc1}z_s = m_1 A_b \Omega^2 \sin(\Omega t),$$

$$c_s\dot{z}_s + (k_s + k_{sc1})z_s - k_{sc1}z_{m1} + k_s x_s^{st} - k_{sc1}z_{sc1}^{st} = 0,$$
$$m_2\ddot{z}_{m2} + (c_{Ls2} + c_{p2})\dot{z}_{m2} + (k_{Ls2} + k_{p2})z_{m2} + k_{Ls2}x_{m2}^{st} = -P_2 + m_2 g + m_2 A_b \Omega^2 \sin(\Omega t). \quad (15)$$

And finally, for phase (iv) to occur, $z_{m1} < (z_s - z_{sc1}^{st})$ and $z_{m2} > (z_s - z_{sc2}^{st})$ have to be satisfied simultaneously. The equations of motion are:

$$m_1\ddot{z}_{m1} + (c_{Ls1} + c_{p1})\dot{z}_{m1} + (k_{Ls1} + k_{p1})z_{m1} + k_{Ls1}x_{m1}^{st} = P_1 + m_1 g + m_1 A_b \Omega^2 \sin(\Omega t),$$
$$c_s\dot{z}_s + k_s z_s + k_s x_s^{st} = 0,$$
$$m_2\ddot{z}_{m2} + (c_{Ls2} + c_{p2})\dot{z}_{m2} + (k_{Ls2} + k_{p2})z_{m2} + k_{Ls2}x_{m2}^{st} = -P_2 + m_2 g + m_2 A_b \Omega^2 \sin(\Omega t). \quad (16)$$

Before non-dimensionalising of the above equations of motion, the following simplifying assumptions were made:

$$m_1 \approx m_2 = m, \quad c_{Ls1} \approx c_{Ls2} = c_{Ls}, \quad k_{Ls1} \approx k_{Ls2} = k_{Ls}, \quad k_{sc1} \approx k_{sc2} = k_{sc}.$$

The developed equations of motion (Eqs. (13)–(16)) are now non-dimensionalised by introducing the following non-dimensional variables:

$$\tau = \omega_{Ls}t, \quad X_1 = \frac{z_{m1}}{A_b}, \quad X_2 = X_1' = \frac{\dot{z}_{m1}}{A_b\omega_{Ls}}, \quad X_3 = \frac{z_s}{A_b}, \quad X_4 = \frac{z_{m2}}{A_b},$$

$$X_5 = X_4' = \frac{\dot{z}_{m2}}{A_b\omega_{Ls}}, \quad X_b = \frac{x_b}{A_b} = \sin(\eta_{Ls}\tau),$$

and parameters

$$\omega_{Ls} = \sqrt{\frac{k_{Ls}}{m}}, \quad \xi_{Ls} = \frac{c_{Ls}}{2m\omega_{Ls}}, \quad \omega_s = \sqrt{\frac{k_s}{m}}, \quad \xi_s = \frac{c_s}{2m\omega_s}, \quad \omega_{p1} = \sqrt{\frac{k_{p1}}{m}},$$

$$\xi_{p1} = \frac{c_{p1}}{2m\omega_{p1}}, \quad \omega_{p2} = \sqrt{\frac{k_{p2}}{m}}, \quad \xi_{p2} = \frac{c_{p2}}{2m\omega_{p2}}, \quad \lambda_1 = \sqrt{\frac{k_{p1}}{k_{Ls}}}, \quad \lambda_2 = \sqrt{\frac{k_{p2}}{k_{Ls}}},$$

$$\vartheta = \sqrt{\frac{k_s}{k_{Ls}}}, \quad \varepsilon = \frac{k_{Ls}}{k_{sc}}, \quad \delta_1 = \frac{x_{m1}^{st}}{A_b}, \quad \delta_2 = \frac{x_{m2}^{st}}{A_b}, \quad \Delta_1 = \frac{z_{sc1}^{st}}{A_b}, \quad \Delta_2 = \frac{z_{sc2}^{st}}{A_b},$$

$$\gamma_s = \frac{x_s^{st}}{A_b}, \quad \eta_{Ls} = \frac{\Omega}{\omega_{Ls}}, \quad f_1 = \frac{P_1 + mg}{mA_b\omega_{Ls}^2}, \quad f_2 = \frac{P_2 - mg}{mA_b\omega_{Ls}^2},$$

where $'$ denotes $\mathrm{d}/\mathrm{d}\tau$.

Eqs. (13)–(16) are transformed to a set of the first-order differential equations which can be given for each phase as

Phase (*i*):

$$X_1' = X_2,$$
$$X_2' = -\left(1 + \lambda_1^2 + \frac{1}{\varepsilon}\right)X_1 - (2\xi_{Ls} + 2\xi_{p1}\lambda_1)X_2 + \frac{1}{\varepsilon}X_3 + \eta_{Ls}^2 \sin(\eta_{Ls}\tau),$$
$$X_3' = \frac{1}{2\varepsilon\vartheta\xi_s}X_1 - \left(\frac{1}{\varepsilon\vartheta\xi_s} + \frac{\vartheta}{2\xi_s}\right)X_3 + \frac{1}{2\varepsilon\vartheta\xi_s}X_4,$$

$$
\begin{aligned}
X_4' &= X_5,\\
X_5' &= \frac{1}{\varepsilon}X_3 - \left(1+\lambda_2^2+\frac{1}{\varepsilon}\right)X_4 - (2\xi_{Ls}+2\xi_{p2}\lambda_2)X_5 + \eta_{Ls}^2\sin(\eta_{Ls}\tau).
\end{aligned} \tag{17}
$$

Phase (*ii*):

$$
\begin{aligned}
X_1' &= X_2,\\
X_2' &= -(1+\lambda_1^2)X_1 - (2\xi_{Ls}+2\xi_{p1}\lambda_1)X_2 - \delta_1 + f_1 + \eta_{Ls}^2\sin(\eta_{Ls}\tau),\\
X_3' &= -\left(\frac{1}{2\varepsilon\vartheta\xi_s}+\frac{\vartheta}{2\xi_s}\right)X_3 + \frac{1}{2\varepsilon\vartheta\xi_s}X_4 + \frac{\Delta_2}{2\varepsilon\vartheta\xi_s} - \frac{\vartheta\gamma_s}{2\xi_s},\\
X_4' &= X_5,\\
X_5' &= \frac{1}{\varepsilon}X_3 - \left(1+\lambda_2^2+\frac{1}{\varepsilon}\right)X_4 - (2\xi_{Ls}+2\xi_{p2}\lambda_2)X_5 + \eta_{Ls}^2\sin(\eta_{Ls}\tau).
\end{aligned} \tag{18}
$$

Phase (*iii*):

$$
\begin{aligned}
X_1' &= X_2,\\
X_2' &= -\left(1+\lambda_1^2+\frac{1}{\varepsilon}\right)X_1 - (2\xi_{Ls}+2\xi_{p1}\lambda_1)X_2 + \frac{1}{\varepsilon}X_3 + \eta_{Ls}^2\sin(\eta_{Ls}\tau),\\
X_3' &= \frac{1}{2\varepsilon\vartheta\xi_s}X_1 - \left(\frac{1}{2\varepsilon\vartheta\xi_s}+\frac{\vartheta}{2\xi_s}\right)X_3 + \frac{\Delta_1}{2\varepsilon\vartheta\xi_s} - \frac{\vartheta\gamma_s}{2\xi_s},\\
X_4' &= X_5,\\
X_5' &= -(1+\lambda_2^2)X_4 - (2\xi_{Ls}+2\xi_{p2}\lambda_2)X_5 - \delta_2 - f_2 + \eta_{Ls}^2\sin(\eta_{Ls}\tau).
\end{aligned} \tag{19}
$$

Phase (*iv*):

$$
\begin{aligned}
X_1' &= X_2,\\
X_2' &= -(1+\lambda_1^2)X_1 - (2\xi_{Ls}+2\xi_{p1}\lambda_1)X_2 - \delta_1 + f_1 + \eta_{Ls}^2\sin(\eta_{Ls}\tau),\\
X_3' &= -\frac{\vartheta}{2\xi_s}X_3 - \frac{\vartheta\gamma_s}{2\xi_s},\\
X_4' &= X_5,\\
X_5' &= -(1+\lambda_2^2)X_4 - (2\xi_{Ls}+2\xi_{p2}\lambda_2)X_5 - \delta_2 - f_2 + \eta_{Ls}^2\sin(\eta_{Ls}\tau).
\end{aligned} \tag{20}
$$

Again the Heaviside step function was used to describe the piecewise nature of the system by defining a set of switch functions G_3 and G_4,

$$
\begin{aligned}
G_3 &= G_3(X_1, X_3) = H(X_1 - (X_3 - \Delta_1)),\\
G_4 &= G_4(X_3, X_4) = H(-X_4 + (X_3 - \Delta_2)).
\end{aligned} \tag{21}
$$

In Eq. (21), when m_1 loses contact with the specimen ($X_1 < (X_3 - \Delta_1)$) the function G_3 is equal to 0, and when m_2 loses contact with the specimen ($X_4 > (X_3 - \Delta_2)$) the function G_4 is equal to 0; otherwise they are equal to 1. The equations of motion that describe all the possible phases are:

$$
\begin{aligned}
X_1' &= X_2,\\
X_2' &= -(1+\lambda_1^2)X_1 - (2\xi_{Ls}+2\xi_{p1}\lambda_1)X_2 - \frac{G_3}{\varepsilon}(X_1 - X_3 + \Delta_1) - \delta_1 + f_1 + \eta_{Ls}^2\sin(\eta_{Ls}\tau),\\
X_3' &= \frac{G_3}{2\varepsilon\vartheta\xi_s}(X_1 - X_3 + \Delta_1) + \frac{G_4}{2\varepsilon\vartheta\xi_s}(-X_3 + X_4 + \Delta_2) - \frac{\vartheta}{2\xi_s}X_3 - \frac{\vartheta\gamma_s}{2\xi_s},\\
X_4' &= X_5,\\
X_5' &= -(1+\lambda_2^2)X_4 - (2\xi_{Ls}+2\xi_{p2}\lambda_2)X_5 - \frac{G_4}{\varepsilon}(-X_3 + X_4 + \Delta_2) - \delta_2 - f_2 + \eta_{Ls}^2\sin(\eta_{Ls}\tau).
\end{aligned} \tag{22}
$$

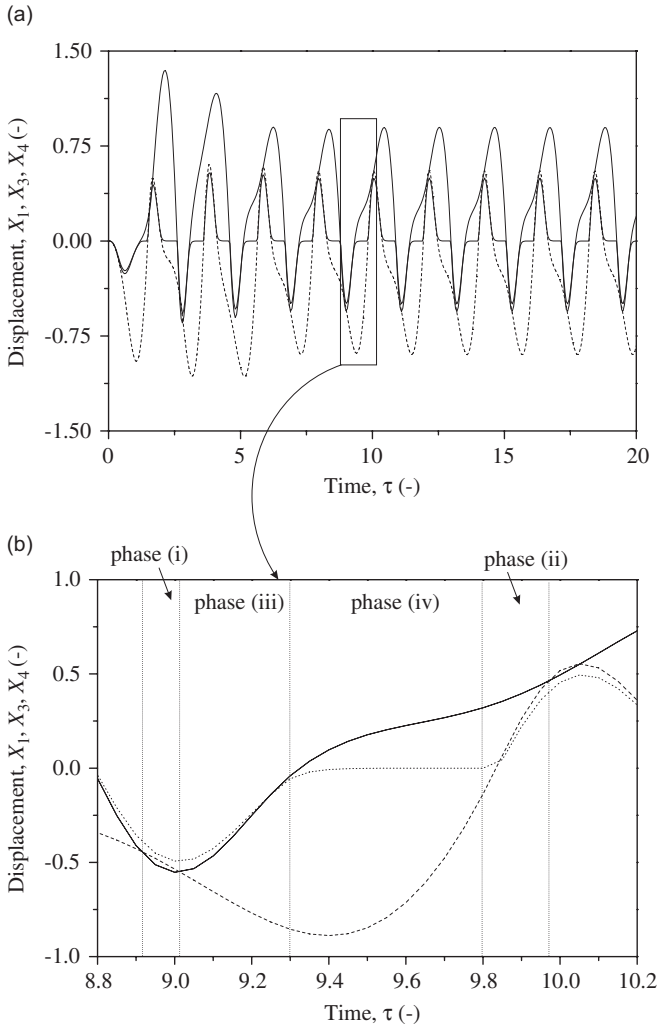

Fig. 8. Time histories computed for $\eta_{Ls} = 3$, $\xi_{Ls} = 0.00255$, $\xi_s = 0.002$, $\xi_{p1} = 0.4$, $\xi_{p2} = 0.4$, $\lambda_1 = 2$, $\lambda_2 = 2$, $\vartheta = 7.828$, $\varepsilon = 0.002012$, $f_1 = 3.75, f_2 = 3.75$. Thick solid line represents X_1, dotted line represents X_3 and dash line represents X_4.

Eq. (22) was used to compute the dynamic responses; four phases of motion can be clearly observed in Fig. 8. The displacements of mass 1, X_1, and mass 2, X_4, are plotted by thick solid and dashed lines, respectively. The displacement of the specimen, X_3, is plotted as dotted line.

Referring to Fig. 8b, at the instant when m_1 hits m_2, both masses are kept in contact with the specimen for a very short time (labelled as phase(i)). Because of the relative displacements of the pre-compressed springs k_{sc1} and k_{sc2}, displacements X_1 and X_4 cross each other in phase (i). After this short period of light impact, due to the energy transfer between m_1 and m_2, m_2 starts to separate while m_1 still follows the trajectory of the specimen (labelled as phase (iii)). When m_1 moves up to the vicinity of the equilibrium point, phase (iv) begins. At this phase, the displacement of the specimen decays and remains stationary as at the equilibrium position. When the position of m_2 coincides with the position of the specimen phase (ii) occurs, in which m_2 moves in phase with the specimen while m_1 is still detached from the specimen.

Numerical and experimental results showing intermittent contacts between the masses and the specimen are compared in Fig. 9. The theoretical steady-state time history for the base acceleration X_b'' is shown in Fig. 9a, while the accelerations of mass 1, X_1'' (thick solid line) and mass 2, X_4'' (thin solid line) are depicted in Fig. 9c. The displacements of mass 1, X_1 (thick solid line), mass 2, X_4 (thin solid line) and of the specimen, X_3 (dotted line) are plotted on the same graph as shown in Fig. 9e. The numerical integrations were performed with zero

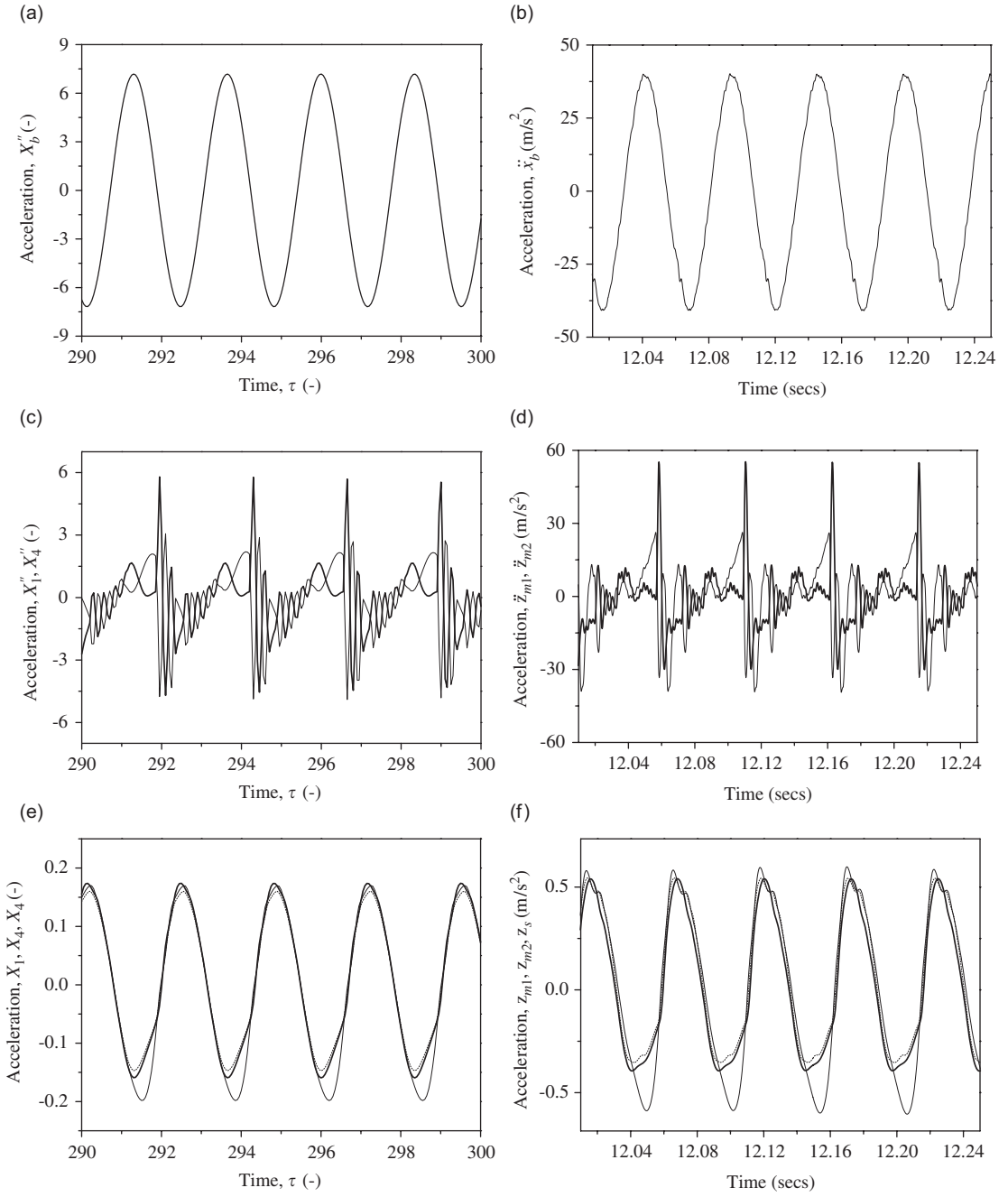

Fig. 9. (a), (c) and (e) Theoretical time histories for $\eta_{Ls} = 2.5$, $\xi_{Ls} = 0.00255$, $\xi_s = 0.002$, $\xi_{p1} = 0.4$, $\xi_{p2} = 0.4$, $\lambda_1 = 4.36$, $\lambda_2 = 4.36$, $\vartheta = 7.828$, $\varepsilon = 0.002012$, $f_1 = 5.44$, $f_2 = 3.52$; (b), (d) and (f) Experimental time histories for excitation frequency of 19.15 Hz and an amplitude of 2.8 mm. Thick solid line represents X_1'', $\ddot{z}_{m1}$, X_1 and z_{m1} and thin solid line represents X_4'', $\ddot{z}_{m2}$, X_4 and z_{m2} in Figs. 9(c), (d), (e) and (f). Dotted line represents X_3 and z_s in Figs. 9(e) and (f).

initial conditions for the following values of the system parameters: $\eta_{Ls} = 2.5$, $\xi_{Ls} = 0.00255$, $\xi_s = 0.002$, $\xi_{p1} = 0.4$, $\xi_{p2} = 0.4$, $\lambda_1 = 4.36$, $\lambda_2 = 4.36$, $\vartheta = 7.828$, $\varepsilon = 0.002012$, $f_1 = 5.44$, $f_2 = 3.52$. The experimental time histories are depicted in Figs. 9b, d and f. The excitation frequency and amplitude used for this experiment were 19.15 Hz and 2.8 mm, respectively. In these figures, Fig. 9b shows the base acceleration $\ddot{x}_b$ where Fig. 9d depicts the relative accelerations $\ddot{z}_{m1}$ (thick solid line) and $\ddot{z}_{m2}$ (thin solid line), and Fig. 9f shows

the relative displacements z_{m1} (thick solid line), z_{m2} (thin solid line) and z_s (dotted line). The relative displacements of m_1 and m_2 were obtained by double numerical integration of the relative accelerations, $\ddot{z}_{m1}$ and $\ddot{z}_{m2}$, respectively.

It can be concluded that good qualitative and quantitative agreements between the theoretical and experimental results have been achieved even though the correlation is not as good as for the single mass model.

3.3. Reduction of two mass model to a single degree-of-freedom system

If the pre-loading forces from the pneumatic cylinders are large enough, both masses and the specimen are always in contact. In this case the system shown in Fig. 7 is described by Eq. (17), and the model can be reduced to a single degree-of-freedom by introducing the following variables:

$$y_1 = \frac{X_1 + X_4}{2}, \quad y_2 = \frac{X_2 + X_5}{2}, \quad y_3 = X_3, \quad z_1 = \frac{X_1 - X_4}{2}, \quad z_2 = \frac{X_2 - X_5}{2}$$

and assuming that

$$\lambda_1 = \lambda_2 = \lambda, \quad \xi_{p1} = \xi_{p2} = \xi_p.$$

Using the new variables, Eq. (17) can be re-written as follows:

$$\begin{aligned}
y_1' &= y_2,\\
y_2' &= -\left(1 + \lambda^2 + \frac{1}{\varepsilon}\right) y_1 - (2\xi_{Ls} + 2\xi_p\lambda) y_2 + \frac{1}{\varepsilon} y_3 + \eta_{Ls}^2 \sin(\eta_{Ls}\tau),\\
y_3' &= \frac{1}{\varepsilon\vartheta\xi_s} y_1 - \left(\frac{1}{\varepsilon\vartheta\xi_s} + \frac{\vartheta}{2\xi_s}\right) y_3,\\
z_1' &= z_2,\\
z_2' &= -\left(1 + \lambda^2 + \frac{1}{\varepsilon}\right) z_1 - (2\xi_{Ls} + 2\xi_p\lambda) z_2.
\end{aligned} \tag{23}$$

As can be seen clearly from Eq. (23), the first three equations do not depend on variable z, while the last two are independent of variable y. Hence two independent systems have been obtained and they can be solved separately. Assuming that $X_1 = X_4$ and $X_2 = X_5$, we have $z_1 = z_2 \equiv 0$, which means that the displacements and the velocities of both masses are equal. Furthermore, for the present system, $k_{sc} \gg k_{Ls}$, and thus, when $\varepsilon \to 0$, it is assumed that the relative displacements and velocities of the springs k_{sc1} and k_{sc2} are negligible. For this case, the displacements of both masses and the specimen are equal. Therefore, the two mass model given in Fig. 7 can be simplified to a single degree-of-freedom model as shown in Fig. 10 and its dynamics can be described by the following equation of motion:

$$M\ddot{z}_M + c_M\dot{z}_M + (k_M + k_s) z_M = MA_b\Omega^2 \sin(\Omega t), \tag{24}$$

where

$$z_M = \frac{z_{m1} + z_{m2}}{2} = z_{m1} = z_{m2}, \quad M = m_1 + m_2,$$

$$c_M = (2c_{Ls} + c_{p1} + c_{p2} + c_s), \quad k_M = (2k_{Ls} + k_{p1} + k_{p2}).$$

Transforming Eq. (24) into the non-dimensional first-order form, we have

$$\begin{aligned}
y_1' &= y_2,\\
y_2' &= -(1 + \kappa_M) y_1 - 2\xi_M y_2 + \eta_M^2 \sin(\eta_M\tau),
\end{aligned} \tag{25}$$

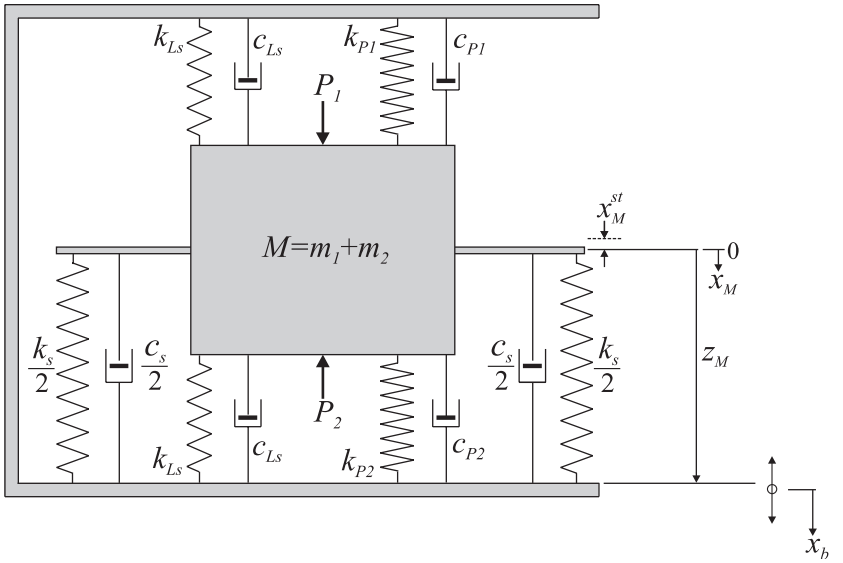

Fig. 10. Simplified single degree-of-freedom model.

whereby the non-dimensional parameters are defined as

$$\tau = \omega_M t, \quad \omega_M = \sqrt{\frac{k_M}{M}}, \quad \xi_M = \frac{c_M}{2M\omega_M}, \quad \kappa_M = \frac{k_s}{k_M}, \quad \eta_M = \frac{\Omega}{\omega_M},$$

where $'$ denotes $\mathrm{d}/\mathrm{d}\tau$.

As has been demonstrated above, when both masses are in contact with the specimen, the set of equations that represent the model in Fig. 7 can be simplified from five first-order equations (see Eq. (23)) to just two (see Eq. (25)). Similarly, for the single mass model (Fig. 4) the equations of motion given in Eq. (5) can be simplified to the same form as Eq. (24), where

$$M = m, \quad c_M = (c_{Ls} + c_p + c_s) \quad \text{and} \quad k_M = (k_{Ls} + k_p).$$

4. Stiffness of a beam with growing fatigue crack

Numerous investigations have been carried out to study the nonlinear effects due to discontinuous stiffness characteristics. For example the externally forced piecewise linear oscillator was studied theoretically by Shaw and Holmes [34], and experimentally by Wiercigroch et al. [35] and Sin and Wiercigroch [36]. The results [34–36] revealed complex dynamics that included the existence of periodic, subharmonic and chaotic motion. Bilinear or piecewise linear oscillators have also been used to model the dynamic behaviour of cracked structures [16–25]. However, as mentioned elsewhere, the work carried out in [16–25] assumed a stationary fatigue crack, in which, the restoring force of the cracked structure has a stiffness characteristic as shown in Fig. 11a. In the present work, taking into account a growing fatigue crack, the stiffness of the bending specimen decreases as a function of crack length and time when crack opens. When crack closes completely, the stiffness of a crack-free specimen is assumed. The bilinear behaviour of restoring force under varying crack length is shown, schematically, in Fig. 11b. The assumption that the stiffness of a bending specimen is unchanged when a fatigue crack closes is based on the fact that the decrease of bending stiffness is small for a large crack length. Furthermore, Gudmundson [10] showed experimentally that the effect of the crack closing has a small influence on the natural frequencies, making our assumption justified.

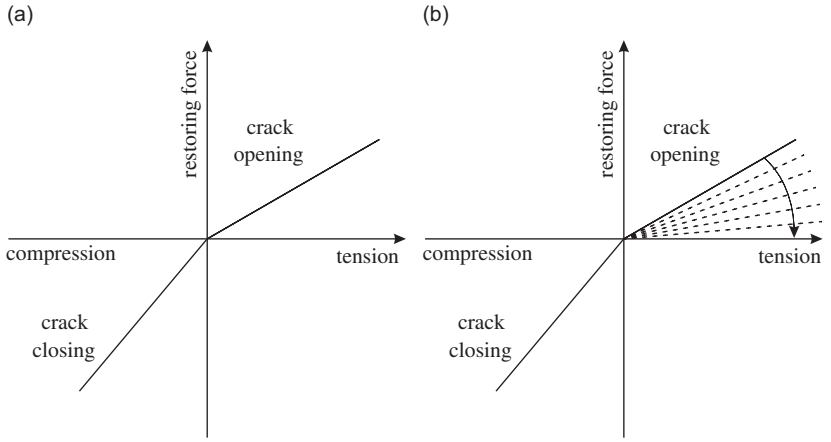

Fig. 11. Stiffness characteristics of a specimen with (a) constant and (b) varying crack length.

The stiffness of the specimen, assumed as a simply supported beam when the crack closes, can be calculated from the formula

$$k_s^{cl} = \frac{48EI}{L_{\text{span}}^3}. \tag{26}$$

When the crack opens, the stiffness k_s^{op} can be computed from Eq. (4), which after a simple rearrangement takes the following form:

$$k_s^{op} = \frac{1}{\dfrac{L_{\text{span}}^3}{48EI} + \dfrac{c_1(\alpha) + \beta c_2(\alpha) + \beta^2 c_3(\alpha)}{EB}}, \tag{27}$$

where all parameters are as defined for Eq. (4). The stiffness k_s^{op} decreases with crack length, a, which can be modelled by an exponential function of time, t, [5], and defined as

$$a = a_0 + a_1 \exp\left(\frac{t - a_2}{a_3}\right), \tag{28}$$

where the constants a_0, a_1, a_2 and a_3 are obtained experimentally. Eq. (28) is used to calculate the crack-depth ratio $\alpha = a/W$ in the functions $c_1(\alpha)$, $c_2(\alpha)$ and $c_3(\alpha)$ of Eq. (27).

During fatigue tests, the two oscillating masses of the fatigue rig were kept in contact with the specimen at all times. The model that represents the full contact case was already presented in Fig. 10 and its equation of motion is given by Eq. (24). Referring to Fig. 10, for the crack to open, the kinematic condition, $(z_M + x_M^{st}) > 0$ must be satisfied, and for the crack to close, $(z_M + x_M^{st}) \leqslant 0$. After including the static forces into Eq. (24) the resulting equation was transformed to a set of non-dimensional first-order equations,

$$\begin{aligned} y_1' &= y_2, \\ y_2' &= -(1 + \kappa_M) y_1 - 2\xi_M y_2 - (\varrho + \kappa_M)\gamma_M + f_M + \eta_M^2 \sin(\eta_M \tau), \end{aligned} \tag{29}$$

where, for the two mass system, parameters ϱ and F_M are:

$$\varrho = \frac{2k_{Ls}}{k_M}, \quad f_M = \frac{P_1 + Mg - P_2}{MA_b\omega_M^2},$$

while for the single mass system,

$$\varrho = \frac{k_{Ls}}{k_M}, \quad f_M = \frac{P + Mg}{MA_b\omega_M^2}.$$

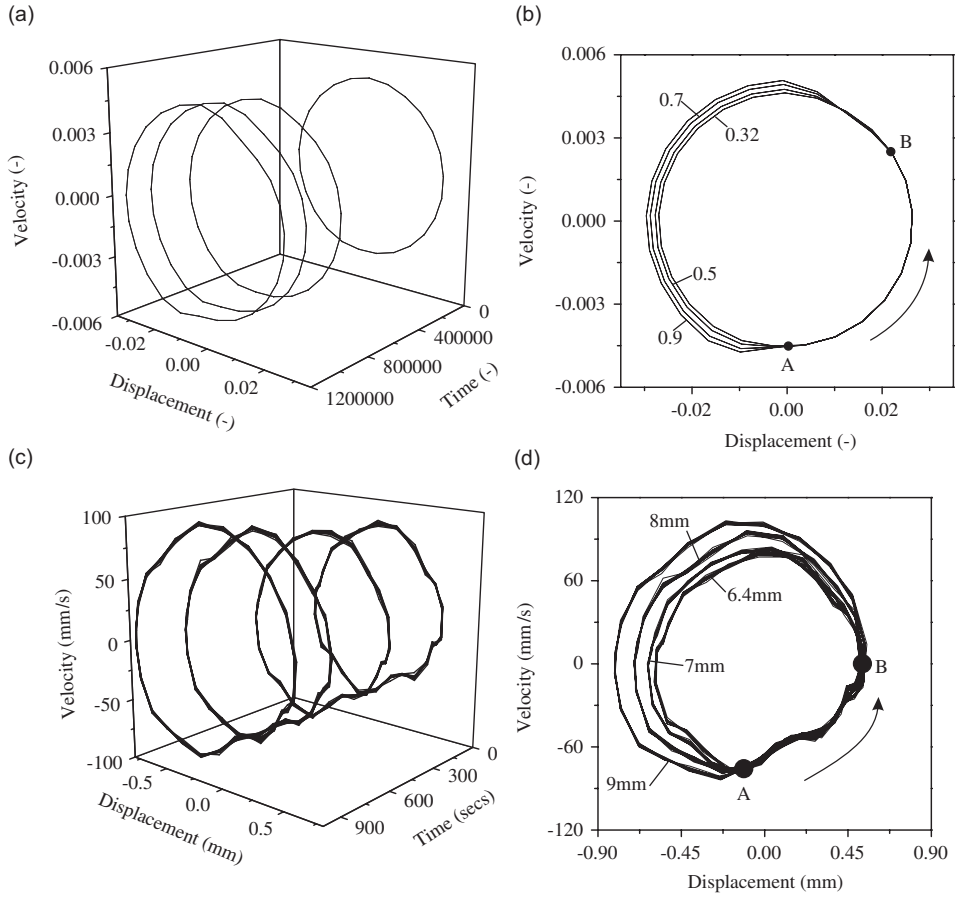

Fig. 12. Phase portraits obtained for 0 N mean load and oscillatory load amplitude of 274 N: (a) theoretical three-dimensional, (b) theoretical two-dimensional, (c) experimental three-dimensional and (d) experimental two-dimensional.

For both systems $\gamma_M = x_M^{st}/A_b$. A Heaviside function $H(y_1 + \gamma_M)$, which is equal to 1 for crack opening and 0 for crack closing is used to model the piecewise linear stiffness characteristics κ_M in Eq. (29), in which

$$\kappa_M = H(y_1 + \gamma_M)\kappa_M^{op} + (1 - H(y_1 + \gamma_M))\kappa_M^{cl}, \tag{30}$$

where

$$\kappa_M^{op} = \frac{k_s^{op}}{k_M}, \quad \kappa_M^{cl} = \frac{k_s^{cl}}{k_M}.$$

Figs. 12a and b depict three dimensional and two dimensional phase portraits representing the dynamic responses of the specimen under a growing breathing crack (crack opens and closes) computed from Eq. (29). The smallest to the largest orbits correspond to the growing crack ratio, α of 0.32, 0.5, 0.7 and 0.9, respectively. All orbits form closed loops indicating period one motion with clearly visible piecewise linear nature of the dynamic responses (see Fig. 12b). This is due to the fact that when the fatigue crack propagates, the stiffness of the specimen decreases when the crack opens, and hence, causes a larger amplitude of oscillations. In addition, the trajectories at different crack lengths follow the same path as the crack closes (point A to B in Fig. 12b), which indicates that the stiffness during crack closure remains constant. These theoretical results have been validated by the experimental phase portraits as shown in Figs. 12c and d.

5. Conclusions

The mathematical modelling and experimental verification of the dynamic interactions for the novel fatigue-testing rig have been presented in this paper. The test rig consists of two, single degree-of-freedom base-excited oscillators, in which one is positioned above and the other below a SENB specimen. During operation, the inertia forces act on the specimen, which is modelled as a discrete element with piecewise nonlinear stiffness. When the crack closes the stiffness of the specimen remains constant; when it opens the stiffness of the specimen decreases as a function of time and crack size. Three dynamic models of the experimental rig were developed to describe different loading and contact scenarios. The theoretical results for the dynamic responses demonstrating *Contact* and *No contact* phases between the oscillators and the crack-free specimen, correlate well with the experiments. This confirms validity of the simplifying assumptions for the dynamic models of the novel testing device.

It was theoretically predicted and experimentally validated that for breathing crack conditions (crack opens and closes), as crack propagates, the amplitude of the oscillations grows for the open crack phases. On the contrary, the amplitude of the oscillations remains the same for the closed crack phases. This finding validates the assumption of constant stiffness when the crack closes.

Acknowledgements

The authors would like to kindly acknowledge financial support from the University of Aberdeen and EPSRC.

References

[1] A. Gupta, R.P. Singh, *Fatigue Behaviour of Offshore Structures*, first ed., Springer, Heidelberg, New York, London, Paris, Tokyo, 1986.
[2] A. Stacey, J.V. Sharp, Fatigue damage in offshore structure—causes, detection and repair, *Journal of Mechanics and Physics of Solids* 3 (1997) 71–79.
[3] Babcock Energy Limited, Assessment of design and operating experience of pipework fatigue in the offshore an petrochemical industries, Technical Report Offshore Technology Report OTI 95/631, HSE Books, 1997.
[4] MSL Engineering Limited, A study of pile fatigue during driving and inservice and of pile tip integrity, Technical Report Offshore Technology Report OTI 2001/018, HSE Books, 2001.
[5] C.H. Foong, E. Pavlovskaia, M. Wiercigroch, W.F. Deans, Chaos caused by fatigue crack growth, *Chaos, Solitons and Fractals* 16 (2003) 1–659.
[6] C.H. Foong, Influence of fatigue crack growth on the dynamics of engineering components and structures, Ph.D. Thesis, University of Aberdeen, 2004.
[7] P.G. Kirmser, Chaos caused by fatigue crack growth, *Proceeding of the American Society of Testing and Materials* 44 (1944) 897–904.
[8] W.T. Thomson, Vibration of slender bars with discontinuities in stiffness, *Journal of Applied Mechanics, Transactions of the ASME* 71 (1949) 203–207.
[9] T.G. Chondros, A.D. Dimarogonas, Identification of cracks in welded joints of complex structures, *Journal of Sound and Vibration* 69 (1980) 531–538.
[10] P. Gudmundson, The dynamic behaviour of slender structures with cross-sectional cracks, *Journal of the Mechanics and Physics of Solids* 31 (1983) 329–345.
[11] A.D. Dimarogonas, C.A. Papadopoulos, Vibration of cracked shafts in bending, *Journal of Sound and Vibration* 91 (1983) 583–593.
[12] C.A. Papadopoulos, A.D. Dimarogonas, Coupling of bending and torsional vibration of a cracked Timoshenko shaft, *Ingenieur-Archiv* 57 (1987) 257–266.
[13] C.A. Papadopoulos, A.D. Dimarogonas, Coupling longitudinal and bending vibrations of a rotating shaft with an open crack, *Journal of Sound and Vibration* 117 (1987) 81–93.
[14] C.A. Papadopoulos, A.D. Dimarogonas, Coupling longitudinal and bending vibrations of a cracked shaft, *Journal of Vibration, Acoustics, Stress, and Reliability in Design, Transactions of the ASME* 110 (1988) 1–8.
[15] C.A. Papadopoulos, A.D. Dimarogonas, Coupled vibration of cracked shafts, in: T.S. Sankar (Ed.), *Rotating Machinery Dynamics*, ASME, DE, 1989, pp. 7–12.
[16] B. Zastrau, Vibration of cracked structures, *Archive of Mechanics* 37 (1985) 736–743.
[17] A. Ibrahim, F. Ismail, H.R. Martin, Modelling of the dynamics of a continuous beam including nonlinear fatigue crack, *International Journal of Analytical and Experimental Modal Analysis* 2 (1987) 76–82.
[18] R.L. Actis, A.D. Dimarogonas, Non-linear effects due to closing cracks in vibration beams, *12th ASME Conference on Mechanical Engineering, Vibration and Noise*, Montreal, Canada, 1989, pp. 99–104.

[19] F. Ismail, A. Ibrahim, H.R. Martin, Identification of fatigue cracks from vibration testing, *Journal of Sound and Vibration* 140 (1990) 305–317.
[20] K.R. Collins, R.H. Plaut, J. Wauer, Detection of cracks in rotating Timoshenko shafts using axial impulses, *Journal of Vibration, Acoustics, Stress, and Reliability in Design, Transactions of the ASME* 113 (1991) 74–78.
[21] K.R. Collins, R.H. Plaut, J. Wauer, Free and forced longitudinal vibrations of a cantilvered bar with a crack, *Journal of Vibration, Acoustics, Stress, and Reliability in Design, Transactions of the ASME* 114 (1992) 171–177.
[22] M.I. Friswell, J.E.T. Penny, A simple nonlinear model of a cracked beam, *10th International Modal Analysis Conference*, San Diego, California, USA, 1992, pp. 516–521.
[23] M.-H.H. Shen, Y.C. Chu, Vibrations of beams with a fatigue crack, *Computers and Structures* 45 (1992) 79–93.
[24] Y.C. Chu, M.-M.H. Shen, Analysis of forced bilinear oscillators and the application to cracked beam dynamics, *AIAA Journal* 30 (1992) 2512–2519.
[25] O.N.L. Abraham, J.A. Brandon, A piecewise linear approach for the modelling of a breathing crack, *17th International Seminar on Modal Analysis*, Leuven, Belgium, 1992, pp. 417–431.
[26] T.G. Chondros, A.D. Dimarogonas, J. Yao, Longitudinal vibration of a bar with a breathing crack, *Engineering Fracture Mechanics* 61 (1998) 503–518.
[27] T.G. Chondros, A.D. Dimarogonas, J. Yao, Vibration of a beam with a breathing crack, *Journal of Sound and Vibration* 239 (2001) 57–67.
[28] T.G. Chondros, A.D. Dimarogonas, dynamic sensitivity of structures to cracks, *Journal of Vibration, Acoustics, Stress, and Reliability in Design, Transactions of the ASME* 111 (1989) 251–256.
[29] T.G. Chondros, The continuous crack flexibility model for crack identification, *Fatigue and Fracture of Engineering Materials and Structures* 24 (2001) 643–650.
[30] A.D. Dimarogonas, Vibration of cracked structures: a state of the art review, *Engineering Fracture Mechanics* 55 (1996) 831–857.
[31] C.H. Foong, M. Wiercigroch, W.F. Deans, Novel dynamic fatigue-testing device: design and measurements, *Measurement Science and Technology* 17 (2006) 2218–2226.
[32] T.L. Anderson, *Fracture Mechanics—Fundamental and Applications*, CRC Press, Boca Raton, AnnArbor, London, Tokyo, 1995.
[33] G.V. Guinea, J.Y. Pastor, M. Elices, Stress intensity factor, compliance and CMOD for a general three-point-bend beam, *International Journal of Fracture* 89 (1998) 103–116.
[34] S.W. Shaw, P.J. Holmes, A periodically forced piecewise linear oscillator, *Journal of Sound and Vibration* 90 (1983) 129–155.
[35] M. Wiercigroch, V.W.T. Sin, Experimental study of base excited symmetrically piecewise linear oscillator, *Journal of Applied Mechanics, Transactions of the ASME* 65 (1998) 657–663.
[36] V.W.T. Sin, M. Wiercigroch, A symmetrically piecewise linear oscillator: design and measurement, *Proceeding of the Institute of Mechanical Engineers Part C* 213 (1999) 241–249.